Chapter 3

Numerical Studies of Shear Banding in Interface Shear Tests using a New Strain Calculation Method

(This paper is coauthored by Jianfeng Wang, Joseph E. Dove and Marte S. Gutierrez)
Dr. Joseph E. Dove is my major advisor and Dr. Marte S. Gutierrez is my co-advisor.

Strain localization is closely associated with the stress-strain behavior of an interphase system subject to quasi-static direct interface shear, especially after peak state is reached. This behavior is important because it is closely related to deformations experienced by geotechnical composite structures. This paper presents a study using two dimensional DEM simulations on the strain localization of an idealized interphase system composed of densely-packed spherical particles in contact with rough manufactured surfaces. The manufactured surface is made up of regular or irregular triangular asperities with varying slopes. A new simple method of strain calculation is used in this study to generate strain field inside a simulated direct interface shear box. This method accounts for particle rotation and captures strain localization features at high resolution. Results show that strain localization begins with the onset of nonlinear stress-strain behavior. A distinct but discontinuous shear band emerges above the surface around peak state, which becomes more expansive and coherent with post peak strain softening. It is found that the shear bands developed by surfaces with smaller roughness are much thinner than those developed by surfaces with greater roughness. The maximum thickness of the intense shear zone is observed to be about 8 to10 median particle diameters above the surface. Theoretical orientations of shear bands are also presented, with Roscoe solution making the best predictions for the major shear band which is aligned with the direction of boundary movement.

KEY WORDS: Interphase, Strain localization, Discrete element methods, Shear band, Surface roughness, Numerical simulations

3.1. Introduction

Shear resistance develops when relative displacement occurs inside the interphase region between a granular soil layer in contact with a natural or manufactured material surface. Strain localization is associated with the stress-strain behavior of the interphase system and results in a series of shear bands developing near the surface, especially after peak state is reached. The mechanism underlying the interphase strength and shear banding behavior is critical to the design of geotechnical composite systems because the load – deformation behavior of the interphase region controls the overall performance of the composite structure. It has been shown by Wang [1] that the evolution of fabric and contact force anisotropy at the boundary between the surface and granular soil controls interphase strength behavior. However, the development of strain localization and shear banding occurring within the interphase region is largely unknown.

3.1.1. Previous related research

Experimental and numerical investigations on the shear bands or rupture surfaces of clayey or granular soils subject to various shearing conditions have contributed to our understanding of shear band morphology. For example, Morgenstern and Tchalenko 1967 studied the formation of small-scale shear features within kaolin subject to direct shear tests. Their observations showed a series of structures and sub-structures were produced in a sequential manner, which coalesce to form the ultimate shear bands. A similar study of shear band patterns on dense sands subject to direct shear was performed by Scarpelli and Wood 1982 using a radiographic technique. Their study showed the important effects of kinematic constraints on the shear banding behavior. Other valuable work on the shear banding behavior of granular soils includes Roscoe 1958, Arthur and Dunstan 1982, Oda et al. 1985, Vermeer 1990, Bardet and Proubet 1992, Alshibli and Sture 2000, Masson and Martinez 2001, etc.

Most of the previous studies on behavior of the interphase between granular media and rough surfaces have focused on exploring and quantifying factors influencing peak and steady state strength (Uesugi and Kishida 1986; Kishida and Uesugi 1987; Dove and Harping 1999; Dove and Jarrett 2002; Paikowsky and Xi 1997). Uesugi and Kishida 1986 introduced a widely used normalized roughness parameter, R_n, correlated with the peak friction angles of sand-steel surfaces. However it has been concluded by the author that traditional geometric surface roughness parameters cannot account for the actual contact conditions occurring at the boundary between the particles and surface, and within the interphase (Refer to Chapter 5 and 6 for more information). Therefore to date, only non-unique correlations with interface strength have been achieved. The author has proposed a failure criterion which is based on the contacts existing between the first layer of particles and the surface. It accounts for the actual mechanism controlling particle and surface interaction and has proven successful in predicting interface strength in a range of particle to surface relative geometries.

However, very limited experimental work has been done on the shear deformation of interphase soils due to difficulty in collecting microscopic information interior to the sample. Uesugi et al. 1988 observed the behavior of sand particles in sand-steel friction in simple shear apparatus and described qualitatively their deformation characteristics due to interface roughness. Westgate and DeJong 2006 used Particle Image Velocimetry (PIV) to investigate the effects of surface roughness, confining pressure and initial void ratio on sand-steel interface shear banding. This study illustrated the key role that surface roughness played on interphase deformation.

The emergence of the Discrete Element Method (DEM) (Cundall 1971; Cundall and Strack 1979) and its numerical simulation provide a powerful tool for studying particulate media and greatly facilitate the understanding of granular micromechanics. A rich body of microscopic information can be obtained from DEM simulations and used to interpret the mechanical behavior in a continuum-based framework (Refer to Chapter 4 for more information). Using DEM simulations, Wang et al. 2005 conducted interface shear box tests composed of densely-packed spherical particles contacting rough manufactured surfaces and suggested a use of sample height of 50 median particle diameters in order for full development of shear band. They also made a preliminary discussion on the effects of surface asperity slope on interphase shear deformation and concluded that the relative grain to surface geometry was the controlling factor of the micromechanical behavior. But these findings are insufficient to provide a quantitative description of the effects of relative grain to surface geometry on interphase shear banding behavior.

3.1.2. Primary work of the current paper

In this paper, a new numerical-based strain calculation method, which is found capable of capturing characteristics of strain localization more accurately than other available methods, is presented and applied to a numerical study to generate strain field inside the interface shear box. Then the numerical model of interface shear test is described and a parametric study is performed to study the influence of relative particle to surface geometry on the shear banding structures within the interphase region. Finally, the results of strain localization evolution, effects of surface geometry and shear band orientation are thoroughly discussed.

3.2. Formulation of Proposed Strain Calculation Method

The spatial discretization approach is the most often used method to compute strains in a discrete system (Thomas 1997; Cambou et al. 2000; Dedecker et al. 2000; Bagi and Bojtar 2001). O'Sullivan et al. 2003 pointed out two problems contributing to inaccurate estimates of strain inside a granular media involving localization: (1) negligence of particle rotation which plays an important role in the formation of shear band, and (2) use of linear local interpolation function which results in erratic inter-element strain values within the shear band.

To avoid the above problems, O'Sullivan et al. 2003 proposed a higher-order, non-local mesh free method which employs a cubic spline interpolation function and takes into account particle rotation and applied the method in their 2D biaxial compression simulations. However, it was found by the authors that the higher-order mesh free interpolation functions do not smooth the displacement gradient satisfactorily within the shear band and thus failed to manifest the strain localization accurately inside the interface shear box. Given this fact, the authors propose herein a modified mesh free method which does not use interpolation functions and calculates the displacement gradient directly based on movements of individual particles. The details of the method are described below.

The current problem involves large strain localization inside the granular media, therefore the Green-St. Venant strain tensor, E_{ij}, is used.

$$E_{ij} = \frac{1}{2}\left(u_{i,j} + u_{j,i} + u_{k,i}u_{k,j}\right), \tag{3-1}$$

where $u_{i,j}$ is the displacement gradient tensor. It is based on the deformation measure related to the reference configuration. Peak or pre-peak shear deformation involves slight degree of strain localization, therefore the second order term in Equation (3-1) can be neglected with little error and the small strain tensor e_{ij} is computed by:

$$e_{ij} = \frac{1}{2}\left(u_{i,j} + u_{j,i}\right) . \tag{3-2}$$

The mesh free method used in this study employs a grid type discretization over the reference configuration. A schematic diagram of the approach is illustrated in Figure 3.1. A rectangular grid is generated that serves as the continuum reference space superimposed over the volume of particles. Then each grid point is assigned to an individual particle *j* which has the following property:

$$\frac{d_j}{r_j} \le \frac{d_i}{r_i} \quad \left(i = 1, 2 \cdots N_p ; i \ne j\right), \tag{3-3}$$

where r_i is the radius of particle *i*; d_i is the distance between the grid point and the centroid of particle *i*; N_p is the total number of particles within the volume [Figure 3.1(a)]. If the ratio of the distance between particle centroid and its associated grid point to the particle radius is the least among all the particles, then the grid point is considered a point on the original or extended rigid body of the particle. Displacement of the grid point is calculated by:

$$\begin{aligned} u_x^g &= u_x^p + d\left(\cos(\theta_0 + \omega) - \cos(\theta_0)\right) \\ u_y^g &= u_y^p + d\left(\sin(\theta_0 + \omega) - \sin(\theta_0)\right) \end{aligned} , \tag{3-4}$$

where u_x^g, u_y^g and u_x^p, u_y^p are the *x* and *y* component of displacement of grid point and particle centroid, respectively; d is the distance between the grid point and the particle centroid; θ_0 is the initial phase angle of the position of grid point relative to the particle centroid; and ω is the accumulated rotation of the particle [Figure 3.1(b)].

This method discretizes the reference space based on the simple algorithm represented by Equation (3-3) before any deformation occurs. Any random point (not necessarily the grid point) inside the whole volume can be assigned to a particular particle using this algorithm. Then all the points that are assigned to the same single particle connect to form a region that belongs to this particle. So if any point lies within this region, it will be considered a point on the original or extended rigid body of this particle, and its displacement will be calculated using the principle of rigid body motion of the particle. The spacing between adjacent grid points is 0.64 mm in the horizontal direction and 0.7 mm in the vertical direction in the current paper. As a general guidance, a grid spacing of a median particle diameter (D_{50}) should suffice to capture the shear localization at satisfactory resolution. This method takes into account the particle rotation. The estimated strain field becomes more accurate with the decreasing grid spacing.

3.3. Numerical Simulation of Interface Shear Test

3.3.1. Numerical model

The DEM model of direct interface shear device was developed by Wang [1] using PFC2D and validated against laboratory data (Dove and Jarrett 2002). The model is made up of a 128 mm long, 28 mm high shear box filled with a polydispersed mixture of spherical particles (maximum and minimum particle diameter 1.05 mm and 0.35 mm respectively) at a low initial porosity (0.12). A sketch of the model is shown in Figure 3.2(a). The lower boundary is made up of a rough surface and two 20 mm long “dead zones” placed at the ends of the box to avoid boundary effects. The rough surface consisted of either regular or irregular triangular asperities, or of profiles of natural and manufactured material surfaces made using a stylus profilometer. There is no particle to boundary friction within the dead zones. Shearing occurs by displacing the lower boundary of the box to the left at a constant velocity of 1 mm per minute. Vertical and horizontal contact forces acting on all the asperities are summed to compute the normal and shear force generated along the interface respectively.

The Hertz-Mindlin contact model was implemented in the simulations. A particle rolling resistance model (Wang et al. 2004) was also applied at both particle-particle contacts and particle-boundary contacts. Physical constants used in the simulations include: Particle density 2650 kg/m^3; shear modulus and Poisson’s ratio of the particles, 29 GPa and 0.3 respectively; critical normal and shear viscous damping coefficient, both equal to 1.0; time step 5.0×10^{-5} sec; particle to surface asperity friction coefficient 0.05; and interparticle and particle-boundary friction coefficient (except the dead zones) during shear, 0.5 and 0.9 respectively.

3.3.2. Parametric study

To systematically study the effects of surface geometry on the interphase shear banding behavior, we conducted five groups of numerical experiments. In Groups 1, 2 and 3, regular saw tooth asperities were used, with asperity height (R_t), asperity width (S_w) and spacing between asperities (S_r) varied in each group respectively [Figure 3.3(a)]. Table 3.1 provides the ranges of variables and constant values in these three groups of experiments. In Group 4, irregular saw tooth asperities are generated randomly and used as the lower boundary [Figure 3.3(b)]. Refer to Chapter 5 for the details of the analytical method and parameters used to generate the irregular surface. In Group 5, profiles of three coextruded geomembrane surfaces are used.

Table 3.1. Variables, constants of surface asperities and their values used in the Experimental Groups 1, 2 and 3.

Group	Variable	Values of Variables	R_t/D_{50}	S_r/D_{50}	S_w/D_{50}
1	R_t/D_{50}	0.1, 0.2, 0.5, 1, 1.2, 1.5, 2, 3, 5	Varied	0	2
2	S_r/D_{50}	0.2, 0.5, 1, 2, 3, 5, 8, 10	1	Varied	2
3	S_w/D_{50}	0.2, 0.5, 1, 2, 3, 4, 5, 10	1	0	Varied

Sixteen evenly-spaced particle columns are identified before shear. Each column is twice the median particle diameter in width and extends for the full height of the specimen. A typical profile of the columns in a 28 mm thick sample is shown in Figure 3.2(b). The displacements and velocities of particles in these columns are recorded during the shearing process and used for analysis of shear banding.

3.4. Results and Discussions

3.4.1. Macro and micromechanical interphase behavior

A typical stress ratio and volume change versus shear displacement relation from Simulation A with $R_t/D_{50} = 1$ in Group 1 is shown in Figure 3.4. Due to the low initial porosity, distinct post peak strain softening to steady state is observed [Figure 3.4(a)]. Significant dilation is also observed [Figure 3.4(b)], with the highest dilation rate occurring around peak state and approaching zero at steady state deformation. Similar curves were obtained from other simulations with varying surface geometries but less dilation and mobilized peak stress ratio is typical for surfaces with lower degrees of relative particle to surface roughness.

The internal shear deformation of the sample is closely monitored by recording the accumulated displacements at different stages of the test of those particles comprising the sixteen selected columns. Snapshots were taken at five instants as indicated on the stress-displacement curve [Figure 3.4(a)]: point A (pre-peak, 0.5 mm), point B (pre-peak, 0.7 mm), point C (peak, 1 mm), point D (post-peak, 2 mm) and point E (steady state, 6.3 mm).

Figure 3.5 shows the profiles of deformed columns inside the shear box at points C, D and E. During initial pre-peak shearing, the sample is deforming uniformly and pure shear distortion is the dominating mode of deformation. With the onset of nonlinear stress-displacement behavior, discontinuities in particle displacements are observed, leading to a narrow, localized shear deformation zone about 10 median particle diameters above the surface asperities. The extent of strain localization is small prior to peak state therefore it cannot be readily observed from columns plots of Figure 3.5(a). After peak state, rolling and sliding of particles over the asperities leads to the rapid reduction of shear stress and expansion of the plastic zone of strain localization. Curved profiles of deformed columns above the asperities can be clearly seen at the post-peak state [Figure 3.5(b)]. At the steady state, a fully developed shear band is presented, which has a higher porosity than the rest part of the sample due to dilation, as shown in Figure 3.5(c).

3.4.2. Evolution of strain localization

The evolution of strain localization can be better visualized by the shear strain contours shown in Figure 3.6. The shear strain field is calculated using the proposed strain calculation method (Equations (3-1)-(3-4)) and is shown overlain on the original configuration of the sample. A series of rupture bands emerge in a sequential way to form the final shear band. The patterns of rupture bands are similar to those observed by Morgenstern and Tchalenko 1967, and Scarpelli and Wood 1982. Here, we adopt the same notation for rupture bands, S_k, as used by Scarpelli and Wood 1982 to describe the evolution of strain localization inside the interface shear box. The subscript k refers to the order of appearance of the rupture bands in time. A sub-structure of a main structure of ruptures S_k is denoted by S_{kb}.

Strain localization occurs very early with the appearance of rupture S_1 at the both ends of the rough surface at about 0.5 mm displacement [Figure 3.6(a)]. But the two S_1 ruptures show different orientations: the one at the right end (passive zone) is making an angle of 26° with the horizontal, while the other one at the left end (active zone) is making an angle of 19° with the horizontal. The difference is due to the greater mobilized strength and dilation occurring in the passive region. A S_2 rupture, immediately following the S_1 ruptures, forms horizontally along the rough surface. Due to the kinematic constraint of the boundary movement, this rupture is forced to be aligned with the direction of zero extension line [Figure 3.6(b)]. When the S_2 rupture extends along the surface, a sub-structure of this rupture starts from the horizontal S_2 band and makes similar angles to the horizontal as the S_1 ruptures. This sub-structure is labeled S_{2b} because it is associated with the presence of a S_2 rupture, but it is caused by a similar mechanism as causing the S_1 ruptures. Another sub-structure labeled S_{1b} arises between rupture S_1 and S_{2b}, making much greater angles with horizontal than rupture S_1 at the right end. Finally, a S_3 rupture, which is generated by the displacement discontinuity of the particle column, forms in a nearly horizontal direction at the middle of the box. Here, the parallel S_2 and S_3 ruptures actually form a kink-band, which is the dominant mode of deformation in the production of the major structures (Morgenstern and Tchalenko 1967).

All these main ruptures and their sub-structures expand and connect with each other with continuous shearing, finally resulting in a mound-shaped region of shear localization at peak state [Figure 3.6(c)]. After peak state, rupture bands expand fast with post-peak strain softening, but as can be seen, the S_1 rupture at the right end and S_2 rupture are the most intensely developed rupture bands [Figure 3.6(d)]. The mound region corresponds to the localized zone under the influence of interface shear and is a visual representation of the interphase region. The peak of the mound is located approximately at the middle of the box, with a height of about 25 median particle diameters above the surface. But the most intensely sheared zone at the bottom of the mound is only 8 to 10 median particle diameters thick. In the steady state with large shear displacement, a slender shear zone of intense strain localization close to the surface emerges [Figure 3.6(e)]. Due to the lower resolution necessary for in this plot, the large mound-shaped localization zone shown in earlier stages cannot be visualized.

Shear strain contours at point C, D and E calculated using the method proposed by O'Sullivan et al. 2003 are shown in Figure 3.7 for comparison. Because a high-order mesh free interpolation function was adopted, the characteristics of the rupture bands inside the shear zone, especially at small strain peak and post peak stages, are not visible. The overall shape of the shear zone is also marked. However at steady state, the shear band is in good agreement with Figure 3.6(e).

3.4.3. Effects of sample height on shear band

It has been mentioned in Chapter 2 that the sample height was found to have considerable influence on the micromechanical behavior and shear zone development. This effect is further investigated below by recording the microscopic deformation in a series of simulations with sample height varying from 7 mm to 42 mm. Figure 3.8 shows the horizontal displacement of Column 9 from Simulation A at 1 mm and 2 mm shear displacement. The shear band is a region of large displacement and velocity gradients. At 1 mm shear displacement (around peak state), displacement discontinuities of column particles can be observed, especially for shorter samples, but the overall shear band has not fully developed in the interphase region [Figure 3.8(a)]. At 2 mm shear displacement (post-peak state), a distinct shear band featured with high displacement gradient emerged, as shown in Figure 3.8(b). It suggests that the shear band reaches its full thickness if the overall specimen height is great than 28 mm (40 times the median particle diameter). The maximum shear band thickness is about 7 mm (10 particle diameter) at a 35 mm sample height. When the sample is too thin, all or a large percentage of the particles are involved in the shear distortion and have velocity close to that of the moving boundaries. In this case, the shear zone intersects the top boundary and does not fully develop.

However, the pattern of shear deformation remains the same regardless of sample height, which is shown by the displacement profiles in Figure 3.8(b). The shear band is fully developed at this post-peak state. It can be seen that above the shear band, the displacement profiles are inclined at nearly the same slope, which is independent of sample height. Displacement is zero at the top boundary but increases to a maximum at the lower boundary. However, in the thinner samples, the displacement profile is artificially cut off at the top but the deformation pattern remains except for the top particles which lag behind due to high boundary friction.

3.4.4. Effects of surface geometry on strain localization behavior

When the surface geometry changes, it will influence the mobilized interface friction resistance and the associated strain localization behavior. Figures 3.9 and 3.10 show the shear strain distributions at peak state and steady state respectively from six simulations with varying surface geometries. These surfaces include: surface B in Group 3 with $S_w/D_{50} = 10$, surface C in Group 1 with $R_t/D_{50} = 5$, surface D in Group 2 with $S_r/D_{50} = 5$, surface E and F in Group 4 (two analytically generated irregular surfaces) and surface G in Group 5 (coextruded geomembrane surface). Profiles of surface geometry of all the six surfaces are shown in Figure 3.11.

It can be seen from Figures 3.9(a), (b) and (c) that the shear localization zones developed by regular saw tooth surfaces at peak state are generally more continuous and expansive than those by irregular surfaces [Figures 3.9(d), (e) and (f)]. This is attributed to the relatively large spatial variation of surface roughness of the irregular surface. Higher mobilized friction resistance will take place at the sections with greater roughness and correspondingly, more intense shear deformation will occur at the same place. Generally speaking, the surfaces which can sustain higher stress ratios will result in greater shear deformation and thicker shear band. The structures of local rupture bands developed by irregular surfaces are also more complicated than those by regular surfaces. Local mound-shaped localization zones are more likely to form at different sections of the irregular surface, with the size of the 'mound' corresponding to the roughness of that particular section of the surface. However, within each local mound-shaped zone, the structure of rupture bands is similar to that of a regular surface, as described above.

In Figure 3.10, the six fully developed shear bands at steady state possess the same general shape but apparently the two shear bands developed by surface B and E [Figures 3.10(a) and (b)] are much more diffuse than the others. This is because the peak stress ratios measured on surface B and E are 0.215 and 0.3 respectively, much lower than the strength ratio (0.63) of the granular material. For surfaces with roughness high enough to fully mobilize the material strength, such as surface A [Figure 3.7(e)] and surface C [Figure 3.10(b)], the shear band thickness reaches its maximum value of about 8 median particle diameters.

However, as mentioned above, the excessively large displacement gradient close to the rough surface at steady state has dwarfed the relatively small displacement discontinuity in the higher region away from the surface when shear localization first appears around peak state. To better examine the scope of shear localization, displacement profiles of column 9 recorded at post-peak state (2 mm shear displacement), which is located at the middle of the box, are shown in Figure 3.12. We can see from Figure 3.12 that surface A and C resist greater shear deformation than other surfaces. In fact, they are also the two surfaces sustaining highest stress ratios (fully mobilizing the material strength). A few particles are trapped inside their asperity valleys and travel nearly the same amount of distance as the surfaces. It is found that surfaces which have great enough roughness to fully mobilize the granular material strength will develop the thickest shear band. The maximum thickness of the shear band due to post-peak localization is about 8 to 10 median particle diameters from the surface asperities. Surfaces with lower degrees of roughness will sustain lower stress ratio and accordingly, develop less intense and thick shear band.

A comparison between the simulation results of particle horizontal displacements and laboratory data by Westgate and DeJong 2006 is shown in Figure 3.13. The simulation data are particle displacements of column 9 from surface B and surface H ($S_w/D_{50} = 3$, Group 3) recorded at 7 mm shear displacement. The laboratory data were obtained from two types of sand-steel interfaces, namely sandblasted surface and epoxied sand-steel surface, but are the average positions and displacements for each row of the PIV patch mesh (21 rows by 28 columns) recorded at the same shear displacement. It can be seen that the profiles of particle displacements from the simulations agree very well with the laboratory data, showing an excellent match in the shear band. At the top of the box, slip of the whole sample is observed in the laboratory test but zero slip occurs in the simulations. This is because the particle to boundary friction is lower in the laboratory test than in the simulation.

3.4.5. Shear band orientation

In the literature, classical solutions to the shear band orientation include Mohr-Coulumb solution, Roscoe solution, Vardoulakis' bifurcation solution and Arthur solution. In Chapter 4, the author discussed the first two solutions under direct shear conditions in the most general case where non-coaxiality behavior and non-horizontal zero linear extension exist. Below, we show only solutions assuming coaxiality between principal stress and principal strain increment directions.

The Mohr-Coulomb solution assumes a shear band forms in the direction of the planes on which maximum mobilized angle of friction occurs, and gives the orientation of shear band as

$$\theta_C = \frac{1}{2}\left(\phi_p - \psi_p\right), \tag{3-5}$$

where, θ_C is the angle between the shear band and the horizontal direction; ϕ_p is the maximum mobilized angle of friction (plane strain friction angle) and ψ_p is the peak dilation angle. This solution provides static requirements for the shear band to form. The Roscoe solution, on the other hand, treats the shear band as a layer of intensely shearing material which coincides with the zero extension line. In this case, the angle α between the shear band orientation and the direction of major principal strain increment can be expressed as

$$\alpha = \pi/4 - \psi_p/2. \tag{3-6}$$

If we denote the angle between the major principal strain increment direction and the horizontal as β, then the angle θ_R that the shear band makes with the horizontal is

$$\theta_R = \beta - \left(\pi/4 - \psi_p/2\right). \tag{3-7}$$

When applied to the major structure of the shear bands (mainly S_2 band), this solution would suggest that the shear band is coincident with the horizontal, a result due to the kinematic requirement for the zero extension line to be aligned with the direction of lower boundary movement. However, local rupture bands (such as S_1, S_{1b} and S_{2b} bands) could take different orientations when zero extension direction deviates from the horizontal. Using bifurcation theory that treats shear band formation as an instability phenomenon, Vardoulakis 1980 obtained a more comprehensive form of solution as follows,

$$\theta_V = \frac{1}{2}\left(\zeta - \psi_p\right). \tag{3-8}$$

Where, θ_V again is the angle between the shear band and the horizontal direction; and

$$\sin\zeta = \frac{\sin\left(\phi_p + \psi_p\right)/2}{\cos\left(\phi_p - \psi_p\right)/2}. \tag{3-9}$$

When the difference between ϕ_p and ψ_p is small, Equation (3-7) can be reduced to

$$\theta_V = \theta_A = \frac{1}{4}\left(\phi_p - \psi_p\right), \tag{3-10}$$

which is exactly the same form as Arthur solution 1977 assuming a series of local shear ruptures distributed approximately along the direction of bisector between the maximum stress obliquity and zero extension directions.

Consider first simulation A as an example. The S_2 band is almost coincident with the horizontal, which means the observed shear band orientation $\theta_b = 0^\circ$, as evident in Figure 3.7. The peak friction angle measured at the interface is $\phi_p = 30^\circ$. The average value for the direction of major principal strain increment in the lower half region over the rough surface at peak state is $\beta = 44^\circ$. The average mobilized dilation angle in the same region is $\psi_p = 4.9^\circ$. Then using Equation (3-5)-(3-10) we can calculate the four solutions to be $\theta_C = 12.6^\circ$, $\theta_R = 1^\circ$, $\theta_V = 6.5^\circ$ and $\theta_A = 6.3^\circ$. Similar calculations have been performed for the other six simulations and the results are listed in Table 3.2. It can seen from Figure 3.9 that the major S_2 bands are all nearly horizontally oriented (i.e., $\theta_b = 0^\circ$), except for simulation G, whose S_2 band is interrupted due to varying roughness along the length of the surface. Apparently the Roscoe solution makes the best theoretical predictions for the S_2 band, as expected. The Vardoulakis and Arthur solution overestimate the values of S_2 band orientation because they involve an averaging effect of other rupture bands which make greater angles with the horizontal.

The same analysis was conducted on the local rupture bands occurring at the right end of the surface. To do this, a sampling region with a 1/3 length of the rough surface and a half height of the box was selected at the right end of the surface, in which average directions of major principal strain increment and mobilized dilation angles at peak state were calculated and used to estimate the theoretical orientations of rupture bands in this region. The results for the seven simulations are listed in Table 3.3. In the sampling region, a combination of S_1, S_2, S_{1b} and S_{2b} bands is involved, which interact with one another in a complicated manner, especially for irregular and real surfaces. Therefore, the observed and theoretical orientations only represent the average orientations of these local rupture bands, with the effects of different mechanisms interpreted by different theoretical solutions. We found that for all the cases the Roscoe solutions which try to relate the shear band orientations to the average directions of zero extension in this region, give the overall best predictions. This result indicates that in the interface shear test, the effects of lower surface boundary is predominant and even in the local region, rupture bands tend to form along the directions of zero extension.

Table 3.2. Average observed and theoretical orientations for S_2 shear band (degrees)

Simulation	ϕ_p	ψ_p	β	θ_C	θ_R	θ_V	θ_A
A	30	4.9	44	12.6	1.0	6.5	6.3
B	12.2	8.9	40	1.7	-0.6	0.8	0.8
C	30	4.5	40	12.8	-2.8	6.6	6.4
D	25.8	5.5	40	10.2	-2.3	5.2	5.1
E	16.7	1.6	42	7.6	-2.2	3.8	3.8
F	24.2	2.1	41	11.1	-3.0	5.7	5.5
G	23	7.3	30	7.9	-11.5	4	3.9

Note: the average observed orientation for S_2 shear band is $\theta_b = 0^\circ$ for all the cases.

Table 3.3. Average observed and theoretical orientations for S_1 shear band at the right end of the surface (degrees)

Simulation	θ_b	ϕ_p	ψ_p	β	θ_C	θ_R	θ_V	θ_A
A	15.0	30	8.6	49	10.7	8.3	5.5	5.4
B	0.0	12.2	4.1	44	4.1	1.1	2.0	2.0
C	0.0	30	2.5	42	13.8	-1.8	7.1	6.9
D	8.0	25.8	12.7	47	6.6	8.4	3.3	3.3
E	6.0	16.7	5.2	49	5.8	6.6	2.9	2.9
F	5.0	24.2	8.3	47	8.0	6.2	4.1	4.0
G	30.0	23	12.6	75	5.2	36.3	2.6	2.6

3.5. Conclusions

A numerical study of shear banding behavior in the interface shear test composed of assemblage of densely-packed spherical particles in contact with rough surfaces is presented. This work was motivated by the lack of knowledge about the strain localization phenomenon associated with stress-strain behavior of the interphase system when the rough surface is displaced with respect to the granular soils. Moreover, there is little study on the effects of surface roughness on the interphase deformation.

In this paper, a simple new numerical-based method of strain calculation, which employs a grid type discretization over the volume of whole assemblage and calculates the displacements of each grid point by assigning each grid point to a particular particle, is used in this study to generate strain field inside the interface shear box. This method avoids using any interpolation function which is conventionally adopted in any other numerical method and brings forth a novel concept for strain calculation in a discrete system. The calculated strain filed is found to clearly outline the overall shape of shear localization zone and capture the characteristics of rupture bands more accurately than that calculated using the method proposed by O'Sullivan et al. 2003.

Results show that strain localization starts early with occurrence of nonlinear stress-strain behavior. Discontinuities of particle displacements lead to localized shear deformation into a narrow zone above the surface asperities around peak state. For a regular surface, a series of rupture bands emerge in a sequential way to form the major and subordinate structures of the final shear zone at the post peak stage. The irregular surfaces tend to develop irregular zones of shear localization due to spatial distribution of surface roughness along its surface length, but the structure of rupture bands within each local shear zone is similar to that of a regular surface. It has been found that the surfaces with greater roughness will generally sustain higher stress ratios and develop thicker shear bands. The surfaces which can fully mobilize the material strength will develop the most intense shear band with maximum thickness of about 8 to 10 median particle diameters. This maximum thickness will not occur if the sample height is less than 40 median particle diameters. Analyses of shear band orientation show that the effect of lower boundary movement is dominant, and Roscoe solution gives the best theoretical predictions both in the overall and local interphase regions.

Acknowledgement

This material is based upon work supported by the National Science Foundation under Grant No. CMS-0200949. Any opinions, findings, and conclusions or recommendations expressed in this material are those of the authors and do not necessarily reflect the views of the National Science Foundation.

Notation

The following symbols are used in this paper:

D_{50} = median particle diameter (mm)

d_i = distance between a grid point and the centroid of particle i

D_r = relative density

e_{ij} = small strain tensor

E_{ij} = Green-St. Venant strain tensor

G = particle shear modulus

N_p = total number of particles within the volume

r_i = radius of particle i

R_n = normalized roughness parameter

R_t = asperity height (µm)

R_{tave} = average value of maximum asperity height over a series of assessment lengths, L (mm)

R_{tmax} = maximum accumulated asperity height (mm)

S_k = notation for main rupture bands with subscript k referring to the order of appearance of the rupture bands in time

S_{kb} = notation for subordinate rupture bands with subscript k referring to the order of appearance of the rupture bands in time

S_r = spacing between asperities (mm)

S_w = asperity width (mm)

$u_{i,j}$ = displacement gradient tensor

u_x^g , u_y^g = x and y component of displacement of grid point

u_x^p , u_y^p = x and y component of displacement of particle centroid

α = angle between shear band orientation and direction of major principal strain increment

β = angle between major principal strain increment direction and the horizontal

ϕ_p = maximum mobilized angle of friction (plane strain friction angle)

θ_0 = initial phase angle of the position of grid point relative to the particle centroid

θ_A = Arthur angle of shear band orientation

θ_b = observed shear band orientation

θ_C = Mohr-Coulomb angle of shear band orientation

θ_R = Roscoe angle of shear band orientation

θ_V = Vardoulakis angle of shear band orientation

ψ_p = peak dilation angle

References

Alshibli, K.A, and Sture, S (2000), "Shear Band Formulation in Plane Strain Experiments of Sand," Journal of Geotechnical and Geoenvironmental Engineering, 126(6), 495-503.

Arthur, J.R.F., and Dunstan, T (1982), "Rupture Layers in Granular Media," IUTAM Conference on Deformation and Failure of Granular Materials, Delft, 453-459.

Arthur, J.R.F., Dunstan, T., and Al-Ani, G.A.J.L., and Assadi, A (1977), "Plastic Deformation and Failure in Granular Media," Géotechnique, 27(1), 53-74.

Bagi, K., and Bojtar, I (2001), "Different Microstructural Strain Tensors for Granular Materials," Proc. 4th Int. Conf. Analysis of Discontinuous Deformation, Bicanic (ed.), University of Glasgow, UK, 261-271.

Bardet, J. P., and Proubet, J (1992), "Shear-band Analysis in Idealized Granular Material," ASCE Journal of Engineering Mechanics, 118(2), 397-415.

Cambou, B., Chaze, M., and Dedecker, F (2000), "Change of Scale in Granular Materials," European Journal of Mechanics, Vol. A (Solids), 19, 999-1014.

Cundall PA. A computer model for simulating progressive large scale movements in blocky rocky systems. Proceedings of the Symposium of the International Society of Rock

Mechanics, Nancy, France, 1971, 2(8): 129-136.

Cundall, P. A., and Strack, O. D. L (1979), “A Discrete Numerical Model for Granular Assemblies,” Géotechnique, 29(1), 47-65.

Dedecker, F., Chaze, M., Dubujet, P., and Cambou, B (2000), “Specific Features of Strain in Granular Materials,” Mechanics of Cohesive-Frictional Materials, 5, 173-193.

Dove, J.E., and Jarrett, J.B (2002), “Behavior of Dilative Sand Interface in a Geotribology Framework,” Journal of Geotechnical and Geoenvironmental Engineering, 128(1), 25-37.

Dove, J.E., and Harping, J.C (1999), “Geometric and Spatial Parameters for Analysis of Geomembrane/Soil Interface Behavior,” Proceeding of Geosynthetics, Boston, MA, International Fabrics Association International, Vol. 1, 575-588.

Kishida, H., and Uesugi, M (1987), “Tests of Interface between Sand and Steel in the Simple Shear Apparatus,” Géotechnique, 37(1), 45-52.

Masson, S., and Martinez, J (2001), “Micromechanical Analysis of the Shear band Behavior of a Granular Material,” Journal of Engineering Mechanics, 127(10), 1007-1016.

Morgenstern, N.R., and Tchalenko, J.S (1967), “Microscopic Structure in Kaolin Subjected to Direct Shear,” Géotechnique, 17, 309-328.

Oda, M., Nemat-Nasser, S., and Konishi, J (1985), “Stress-induced Anisotropy in Granular Masses,” Soils and Foundations, 25(3), 85-97.

O’Sullivan, C., Bray, J.D., and Li, S.F (2003), “A New Approach for Calculating Strain for Particulate Media,” Int. J. Num. Analy. Mech. Geomech, 27, 859-877.

Paikowsky, S.G., and Xi, F (1997), “Photoelastic Quantitative Study of the Behavior of Discrete Materials with Application to the Problem of Interfacial Friction,” Research Report, Air Force Office of Scientific Research, Research Grant F49620-93-0267.

Roscoe, K.H., Schofield, A.N., and Wroth, C.P (1958), “On the Yielding of Soils,” Géotechnique, 8(1), 22-53.

Scarpelli, G., and Wood, D.M (1982), “Experimental Observations of Shear Band Patterns in Direct Shear Tests,” IUTAM Conference on Deformation and Failure of Granular Materials, Delft, 472-484.

Thomas, P.A (1997), “Discontinuous deformation analysis of particulate media,” Ph.D. Thesis, Department of Civil Engineering, University of California: Berkeley.

Uesugi, M., and Kishida, H (1986), “Influential Factors of Friction between Steel and Dry

Sands," Soils and Foundations, 26(2), 33-46.

Uesugi, M., and Kishida, H (1986), "Frictional Resistance at Yield between Dry Sand and Mild Steel," Soils and Foundations, 26(4), 139-149.

Uesugi, M., and Kishida, H., and Tsubakihara, Y (1988), "Behavior of Sand Particles in Sand-Steel Friction," Soils and Foundations, 28(1), 107-118.

Vardoulakis, I (1980), "Shear Band Inclination and Shear Modulus of Sand in Biaxial Tests," International Journal for Numerical and Analytical Methods in Geomechanics, 4, 103-119.

Vermeer, P.A (1990), "The Orientation of Shear Bands in Biaxial Tests," Géotechnique, 40(2), 223-236.

Wang, J.F., Dove, J.E., Gutierrez, M.S., and Corton, J.D (2005), "Shear Deformation in the Interphase Region," Powders and Grains 2005 (R. Garcia-Rojo, H.J. Herrmann, S. McNamara, Eds), Stuttgart, Germany, 747-750.

Wang, J.F., Gutierrez, M.S., and Dove, J.E (2005), "Strain Localization in an Idealized Interphase System," Proc. 2005 Joint ASME/ASCE/SES Conf. Mech. Mat., Baton Rouge, Louisiana.

Wang, J.F., Gutierrez, M.S., and Dove, J.E (2004), "Effect of Particle Rolling Resistance on Interface Shear Behavior," Proceedings 17th ASCE Engineering Mechanics Conference, Newark, Delaware, 56-63.

Westgate, Z.J., and DeJong, J.T (2006), "Evolution of Sand-structure Interface Response during Monotonic Shear using Particle Image Velocimetry," Proceedings of Geocongress 2006, ASCE, Atlanta, Georgia.

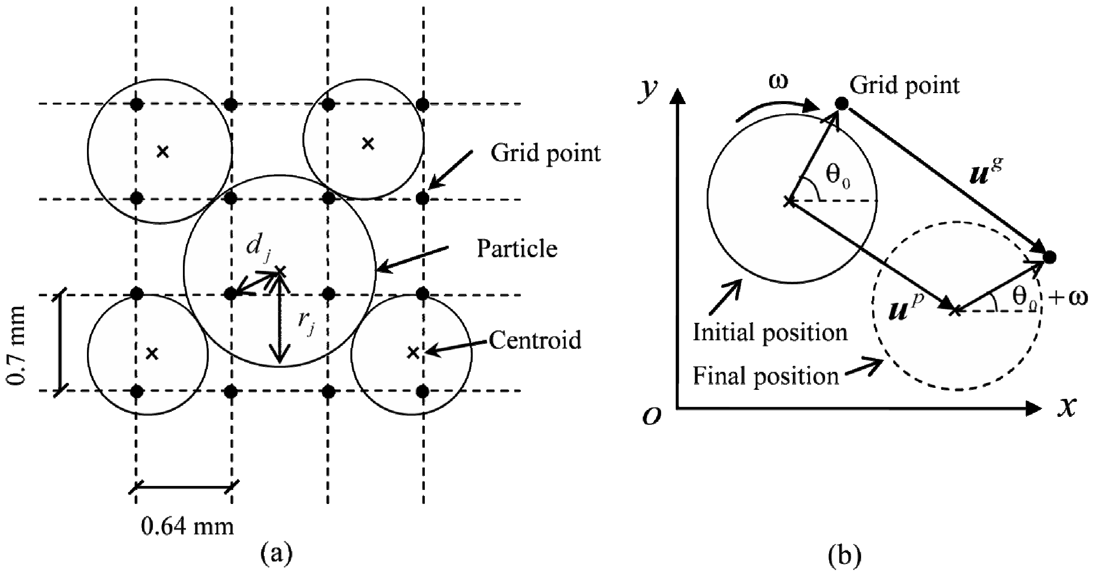

Figure 3.1. Schematic diagram of the new meshfree method: (a) association of a grid point with certain particle; (b) displacement of grid point and its associated particle.

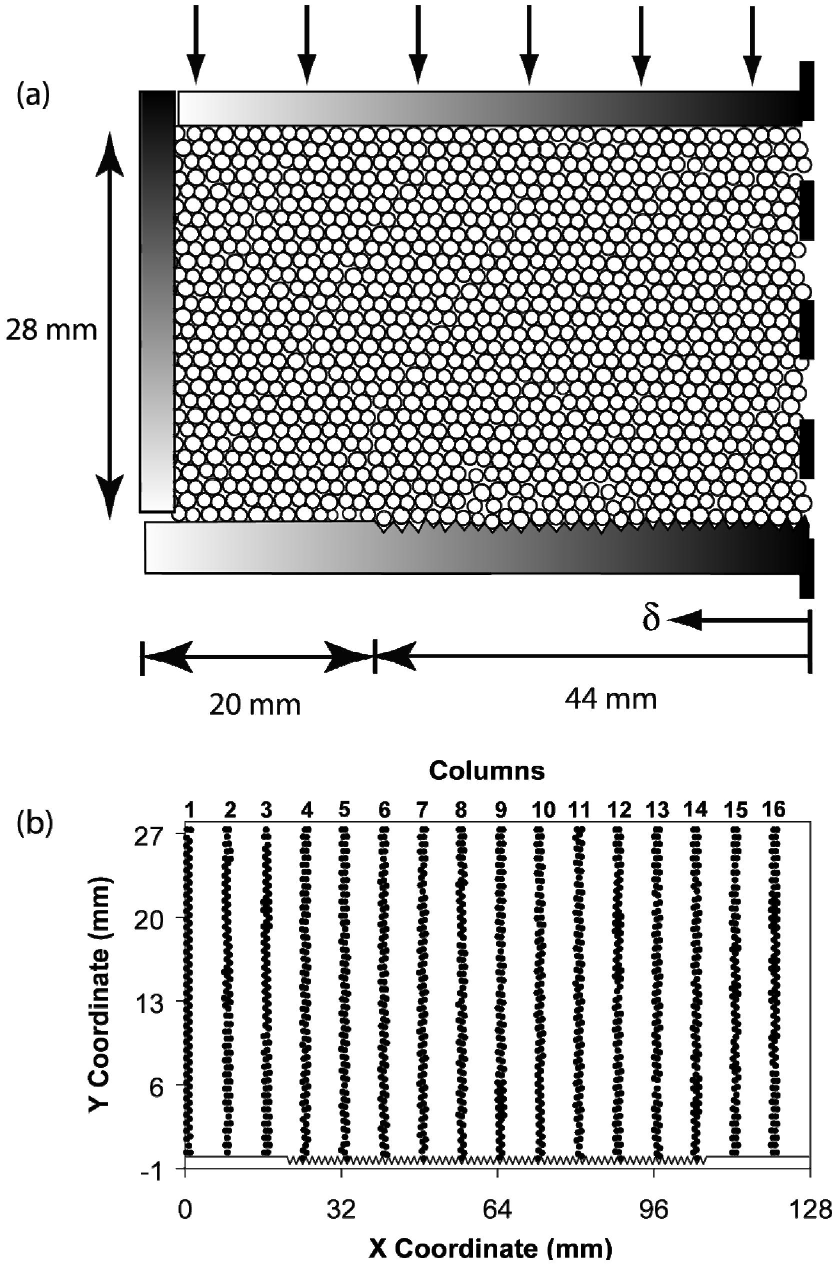

Figure 3.2. DEM model of direct interface shear box: (a) interphase composed of granular spheres in contact with a rough surface; (b) particle columns pre-selected to identify interphase deformation.

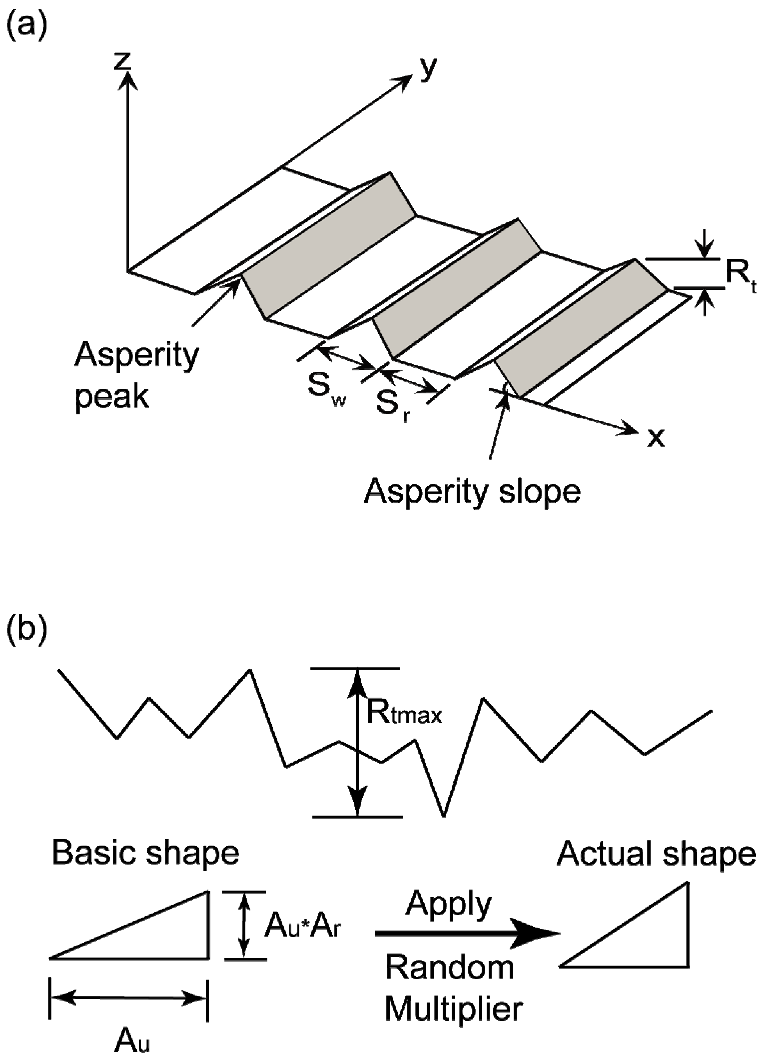

Figure 3.3. (a) Surface geometry used Groups 1, 2 and 3; (b) Group 4. Note extreme roughness of surface.

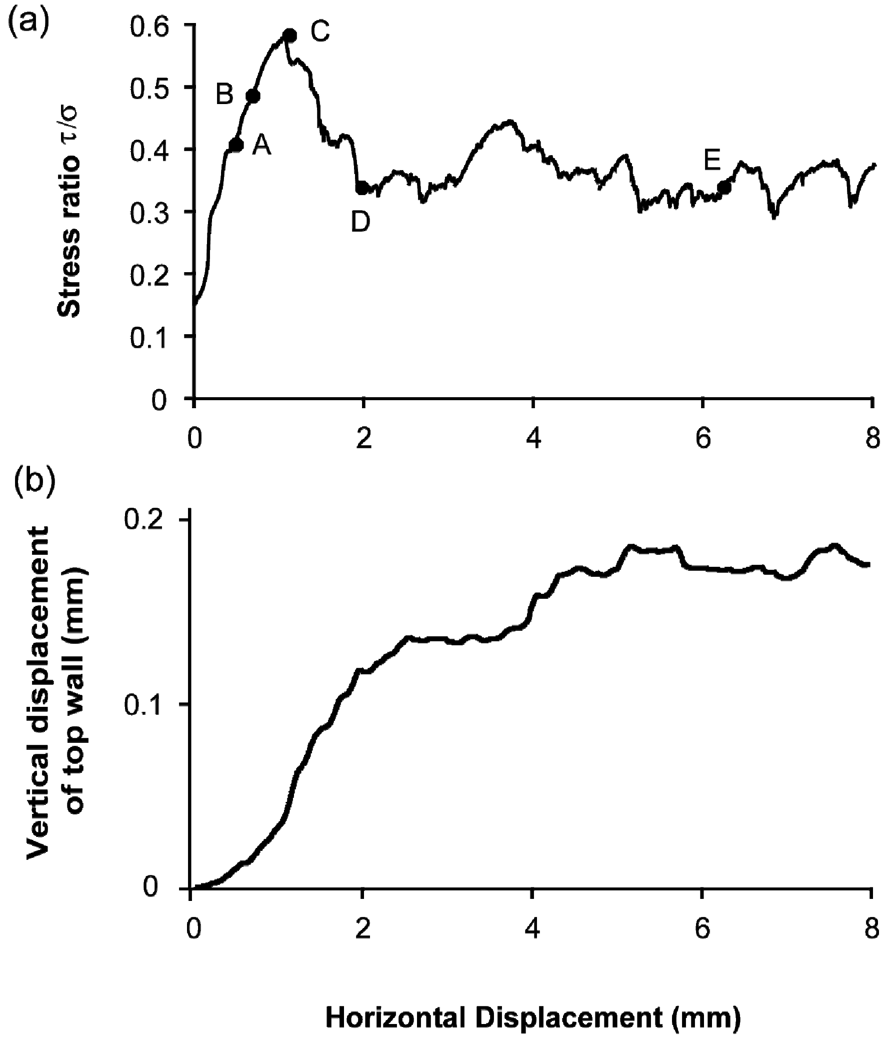

Figure 3.4. Macroscopic interface behavior of Simulation A: (a) stress-displacement relationship; (b) volume change-displacement relationship.

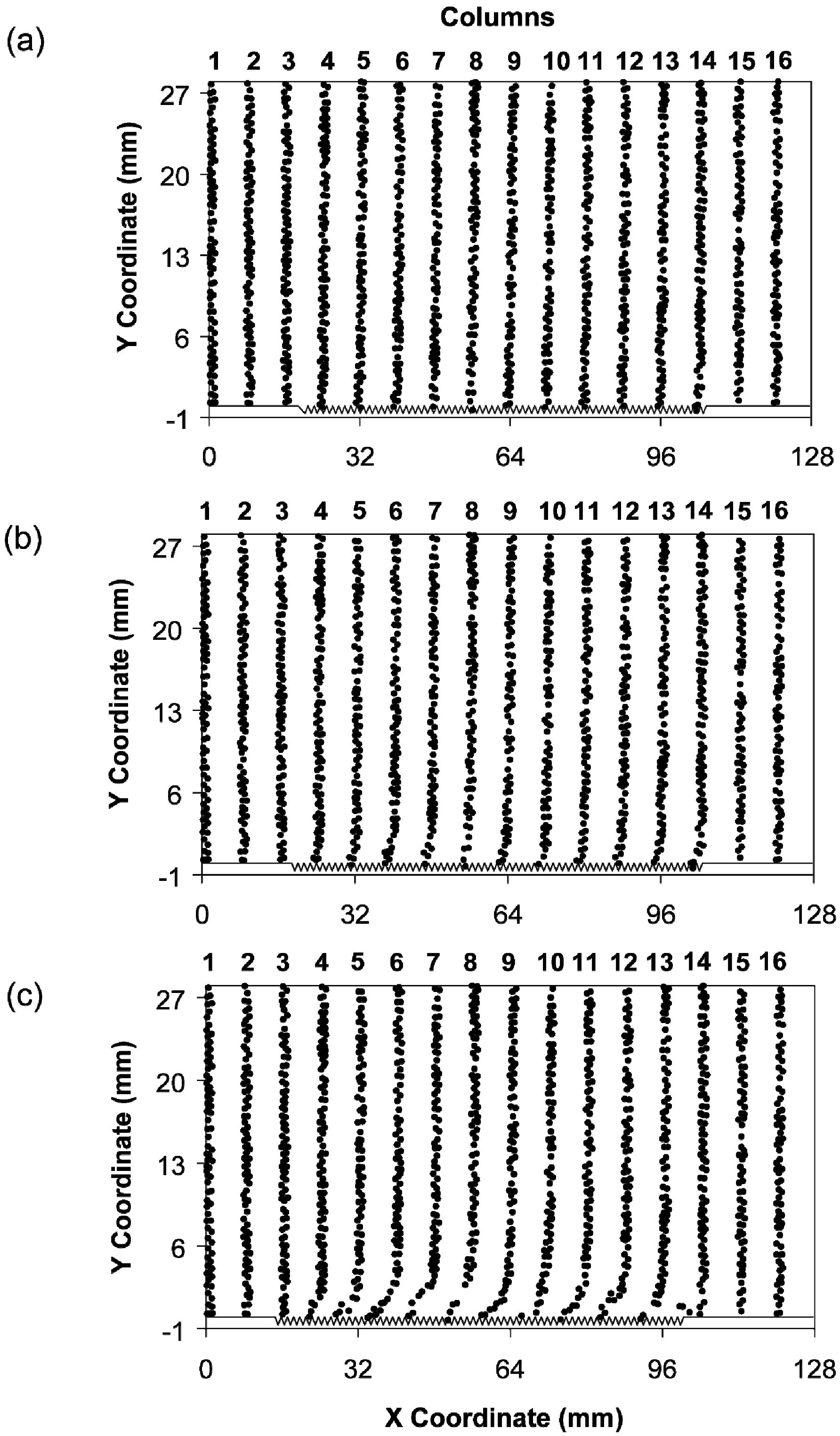

Figure 3.5. Deformed particle columns inside the shear box from Simulation A: (a) at peak, 1 mm displacement; (b) at post-peak, 2 mm displacement; (c) at steady state, 6.3 mm displacement.

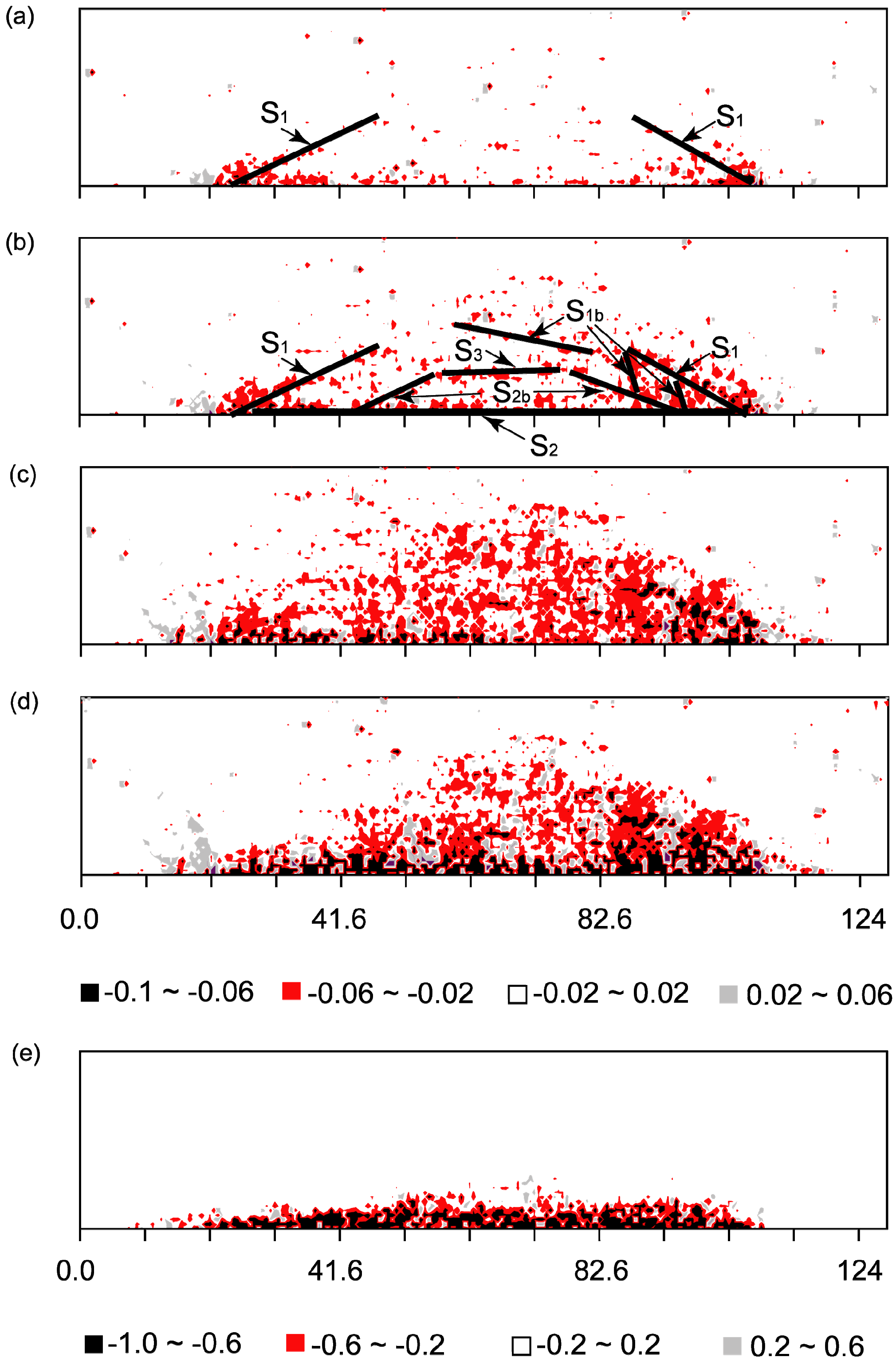

Figure 3.6. Evolution of strain localization and rupture bands in Simulation A: (a) at pre-peak, 0.5 mm displacement; (b) at pre-peak, 0.7 mm displacement; (c) at peak, 1 mm displacement; (d) at post-peak, 2 mm displacement; (e) at steady state, 6.3 mm displacement.

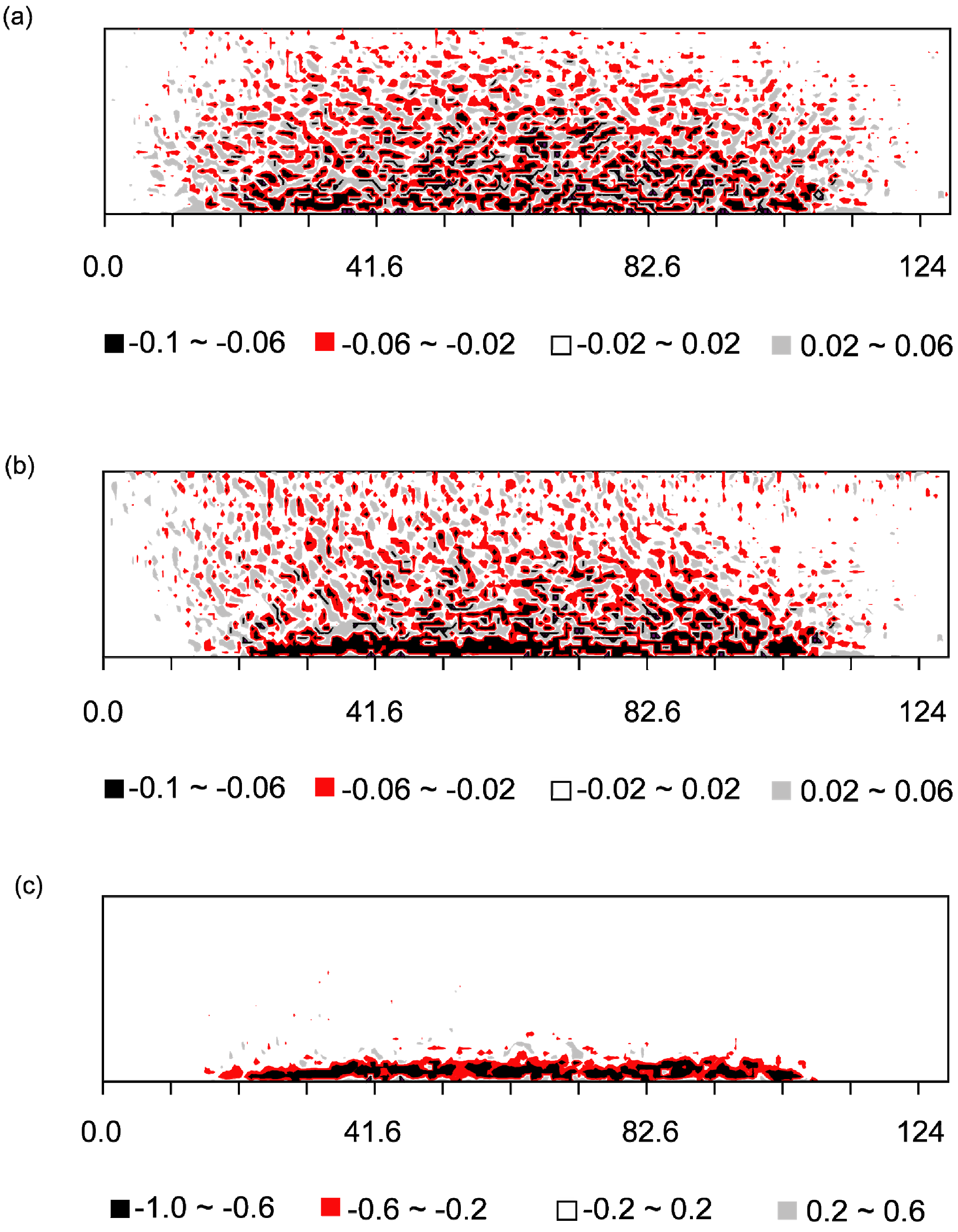

Figure 3.7. Evolution of strain localization in Simulation A calculated using O'Sullivan's method: (a) at peak, 1 mm displacement; (b) at post-peak, 2 mm displacement; (c) at steady state, 6.3 mm displacement.

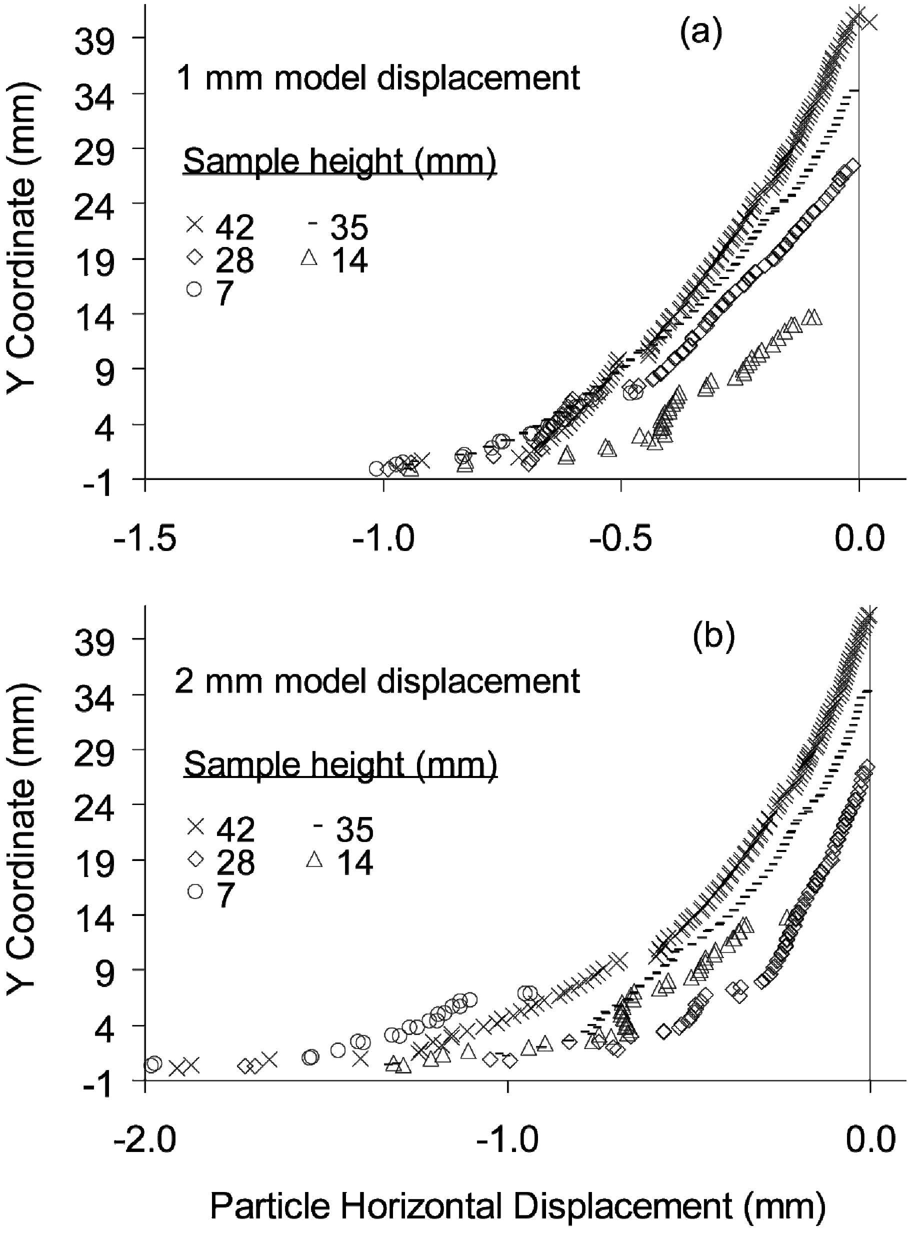

Figure 3.8. Horizontal displacement profiles for selected sample heights, Column 9, Simulation A: (a) 1 mm shear displacement; (b) 2 mm shear displacement.

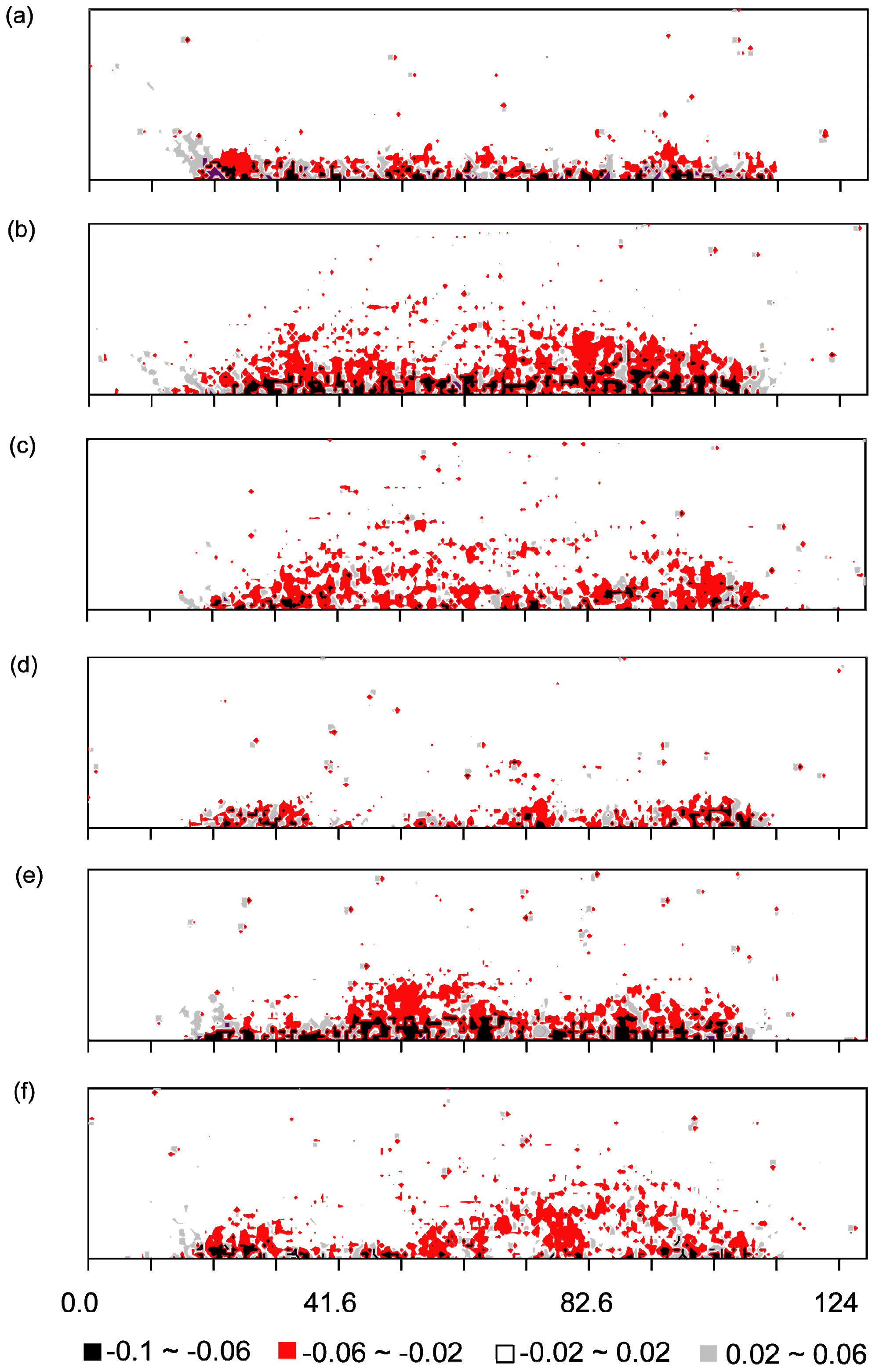

Figure 3.9. Shear strain distribution and rupture bands at peak state in Simulation B to G: (a) Simulation B; (b) Simulation C; (c) Simulation D; (d) Simulation E; (e) Simulation F; (f) Simulation G.

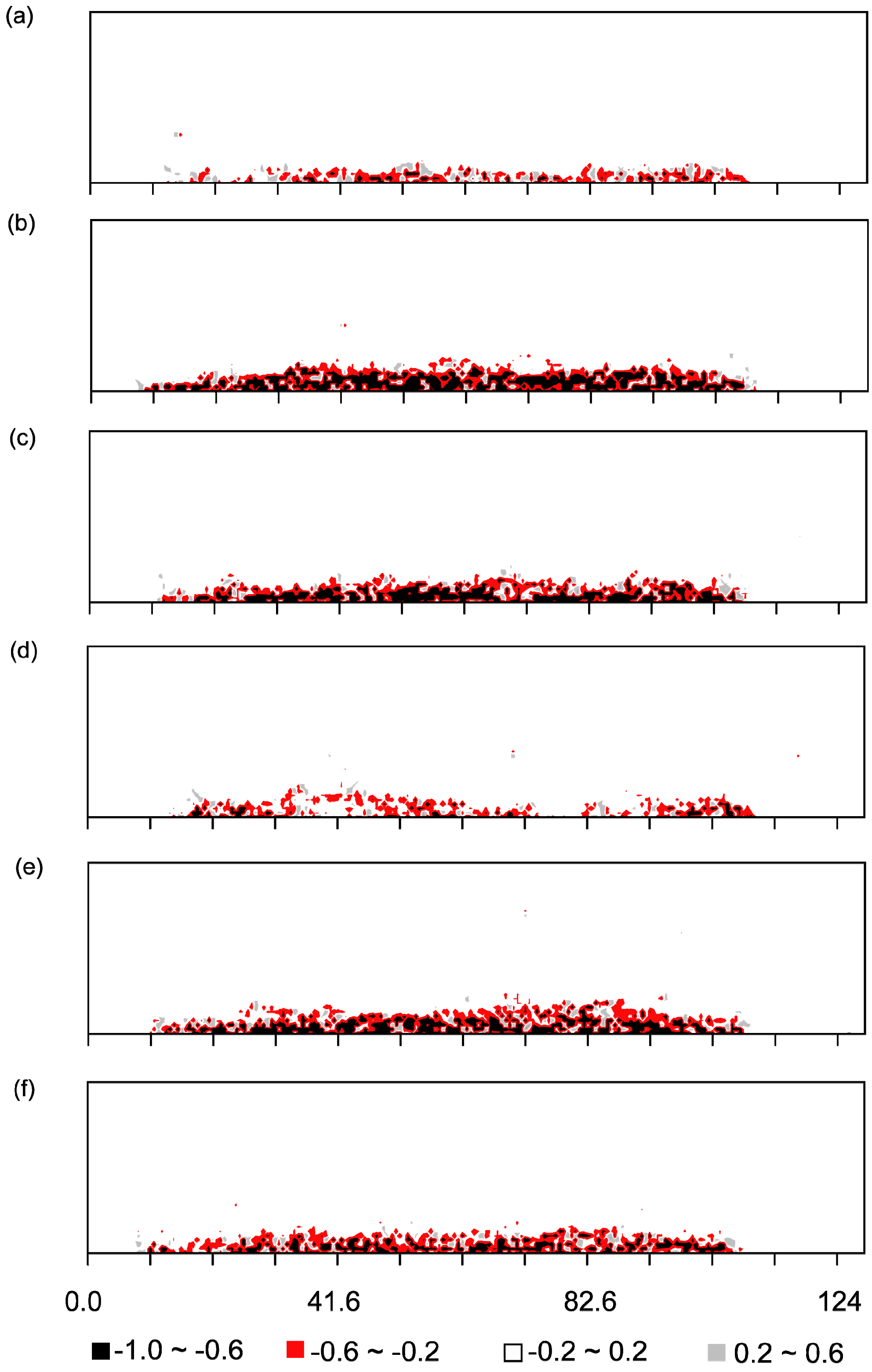

Figure 3.10. Shear strain distribution and rupture bands at steady state in Simulation B to G: (a) Simulation B; (b) Simulation C; (c) Simulation D; (d) Simulation E; (e) Simulation F; (f) Simulation G.

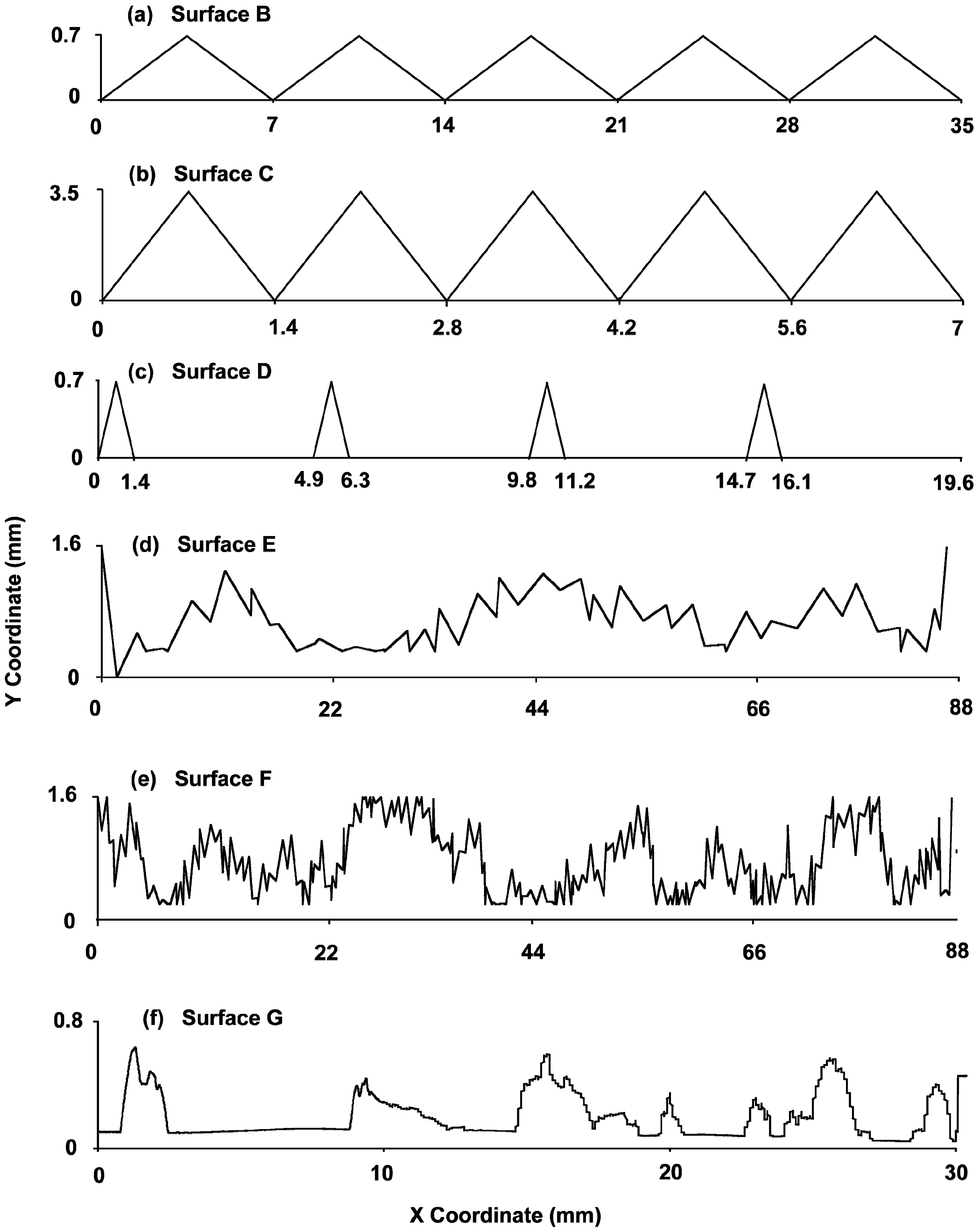

Figure 3.11. Profiles of surface geometry in Simulation B to G: (a) Simulation B; (b) Simulation C; (c) Simulation D; (d) Simulation E; (e) Simulation F; (f) Simulation G.

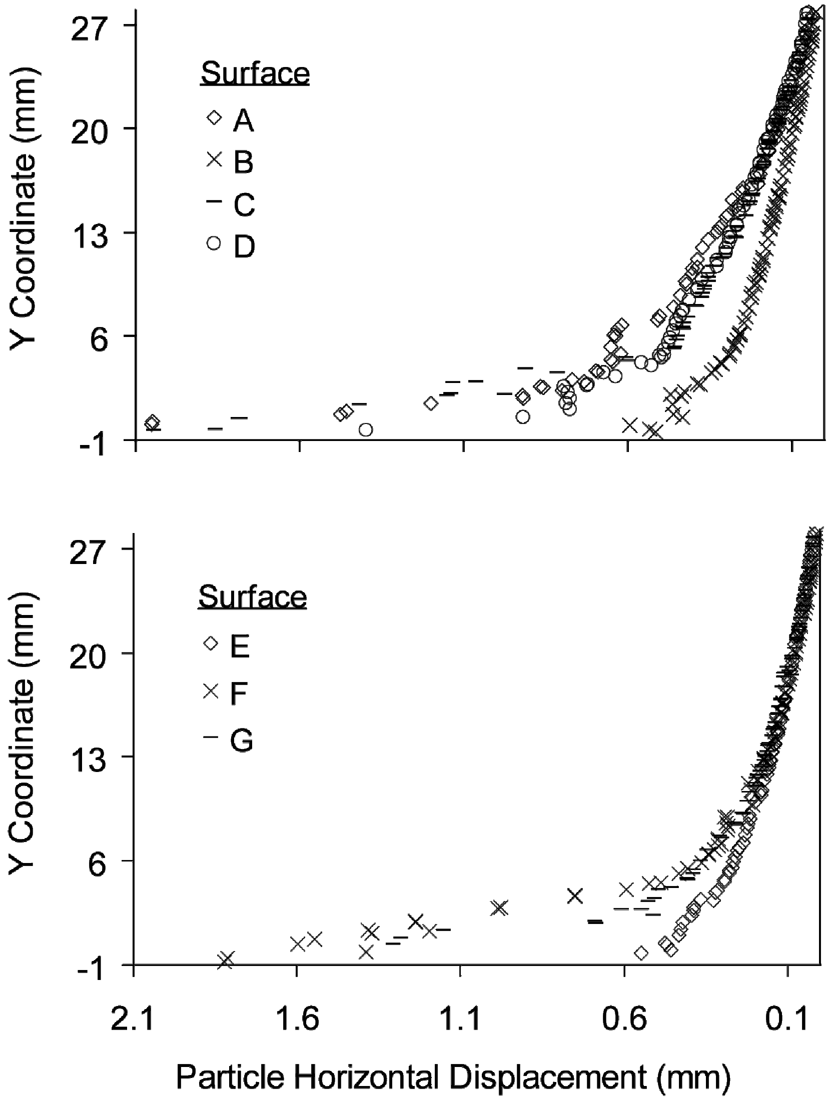

Figure 3.12. Horizontal displacements of particles in Column 9 at 2 mm displacement in Simulation A to G.

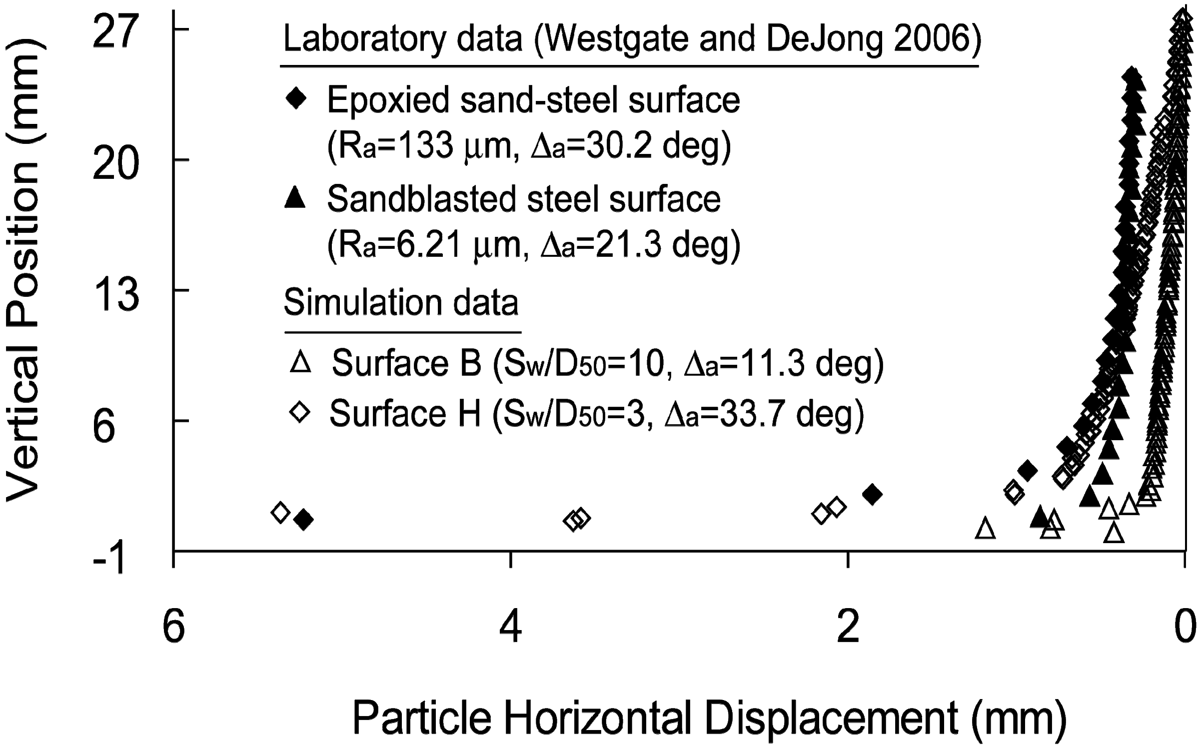

Figure 3.13. Comparison of particle horizontal displacements from simulations with laboratory data.